nent from −45 nT to 40 nT in the geocentric solar magnetospheric (GSM) coordinate system. This coordinate system is defined such that the $X$ axis points from Earth to the Sun, $Y$ is perpendicular to Earth's magnetic dipole axis so that the $XZ$ plane contains the dipole axis, and $Z$ is in the same sense as the northern magnetic pole. For each magnetopause crossing, the magnetospheric density adjacent to the magnetopause was greater than 10 $cm^{-3}$. This is close to two orders of magnitude greater than the nominal value, demonstrating the presence of a plume. The density was measured through the spacecraft potential.

During each of the three magnetopause crossings, a strong rotation of the magnetic field (>120°) and a reconnection jet were observed. These crossings provide several confirmations of magnetic reconnection and the participation of the dense plume in the process. The first confirmation is the jet velocity. The reconnection jet is caused by the magnetic tension force that accelerates the exhaust plasma to the Alfvén speed. In the case of asymmetric reconnection, when the density and magnetic field strength are not the same on both sides of the current sheet, the jet velocity is a hybrid of Alfvén speeds on both sides. In each boundary crossing, the jet velocity matches to within 5% of the predicted hybrid Alfvén speed (Fig. 3) as calculated by a previous model (*9*, *16*).

A second confirmation of the impact of the cold plume plasma is the location of the reconnection jet. Typically the magnetosheath is much denser than the dayside magnetosphere and the jet lies primarily on magnetic field lines with magnetospheric orientation ($+B_L$) (*17*, *18*). In our study, the region of the magnetosphere adjacent to the magnetopause has been mass-loaded and the jets are primarily on field lines with magnetosheath orientation ($-B_L$) (Fig. 3). The occurrence of reconnection jets primarily on field lines of magnetosheath orientation provides additional evidence for the impact of the plume density on magnetopause reconnection.

The location of THEMIS at the reconnecting magnetopause also maps to the point in the ionosphere where the TOI is formed and enhancements in TEC stream tailward over the pole on open field lines (Fig. 1). This confirms that the formation of the TOI in the ionosphere is spatially linked to the presence of the plume and reconnection at the magnetopause. The dense plasma on newly opened magnetic field lines convects tailward over the pole, as observed in the motion of TOI patches in the ionosphere and in situ at the magnetopause. Future studies using the high spatial and almost continuous coverage of the ground-based TEC maps may use this connection to monitor reconnection and identify when plume material has reached the magnetopause.

In addition to identifying substantial density enhancements and mass loading at the magnetopause, these conjugate measurements confirm the connection between intermittent reconnection signatures at the magnetopause and in the ionosphere. Bursts of reconnection can cause twisted magnetic flux ropes known as flux transfer events to form at the magnetopause (*19*, *20*). At the magnetopause, a flux transfer event, demonstrating intermittent or "bursty" reconnection, was observed in the THEMIS measurements (Fig. 4). In the ionosphere, patches of TEC enhancements known as polar cap patches were observed convecting over the pole on open magnetic field lines (Fig. 1). These patches correspond to variability in reconnection causing uneven rates of plasma to be transported over the pole. Previous work (*13*, *14*) used polar cap patches to infer variability in magnetopause reconnection; however, this association had not been validated through in situ measurements at the magnetopause.

Our results imply an extended plasmaspheric plume that spanned from a nominal plasmapause to the dayside magnetopause, where it impacted magnetic reconnection. Ground-based TEC measurements demonstrate that the extended plume existed for several hours. During this period, three THEMIS spacecraft provided magnetically coincident measurements of the plume mass-loading the magnetopause reconnection site near local noon. The spacecraft measurements show signatures of intermittent or bursty reconnection at the magnetopause corresponding to the occurrence of patches of enhanced TEC convecting tailward on open field lines over the pole in the ionosphere. The simultaneous observation of the conjugate location of the reconnection site at the magnetopause with the TEC cusp signature ionosphere (Fig. 1) is important. With this association validated, studies of the occurrence, location, and variability of reconnection at the magnetopause can be conducted with the assistance of ground-based TEC maps that provide high spatial and almost continuous temporal coverage.

## References and Notes


1. C. R. Chappell, K. K. Harris, G. W. Sharp, *J. Geophys. Res.* **75**, 50–56 (1970).
2. C. R. Chappell, K. K. Harris, G. W. Sharp, *J. Geophys. Res.* **76**, 7632–7647 (1971).
3. J. C. Foster, A. J. Coster, P. J. Erickson, F. J. Rich, B. R. Sandel, *Geophys. Res. Lett.* **31**, L08809 (2004).
4. J. C. Foster, P. J. Erickson, A. J. Coster, J. Goldstein, F. J. Rich, *Geophys. Res. Lett.* **29**, 1623 (2002).
5. J. E. Borovsky, M. H. Denton, *Geophys. Res. Lett.* **33**, L20101 (2006).
6. J. E. Borovsky, M. Hesse, *Phys. Plasmas* **14**, 102309 (2007).
7. B. M. Walsh, D. G. Sibeck, Y. Nishimura, V. Angelopoulos, *J. Geophys. Res.* **118**, 4844–4851 (2013).
8. J. E. Borovsky, M. H. Denton, R. E. Denton, V. K. Jordanova, J. Krall, *J. Geophys. Res.* **118**, 5695–5719 (2013).
9. P. A. Cassak, M. A. Shay, *Phys. Plasmas* **14**, 102114 (2007).
10. J. Birn, J. E. Borovsky, M. Hesse, *Phys. Plasmas* **15**, 032101 (2008).
11. J. C. Foster, *J. Geophys. Res.* **98**, 1675 (1993).
12. J. C. Foster *et al.*, *J. Geophys. Res.* **110**, A09S31 (2005).
13. Q. H. Zhang *et al.*, *Science* **339**, 1597–1600 (2013).
14. M. Lockwood, H. C. Carlson Jr., *Geophys. Res. Lett.* **19**, 1731–1734 (1992).
15. V. Angelopoulos, *Space Sci. Rev.* **141**, 5–34 (2008).
16. See supplementary materials on *Science* Online.
17. G. Paschmann *et al.*, *J. Geophys. Res.* **91**, 11099 (1986).
18. A. L. La Belle-Hamer, A. Otto, L. C. Lee, *J. Geophys. Res.* **100**, 11875 (1995).
19. C. T. Russell, R. C. Elphic, *Space Sci. Rev.* **22**, 681 (1978).
20. L. C. Lee, Z. F. Fu, *Geophys. Res. Lett.* **12**, 105–108 (1985).
21. J.-H. Shue *et al.*, *J. Geophys. Res.* **102**, 9497 (1997).
22. P. T. Newell *et al.*, *Ann. Geophys.* **20**, 1039–1047 (2002).


**Acknowledgments:** Supported by NSF grant AGS-1136827. We acknowledge NASA contract NAS5-02099 and instrument teams for use of the data from the THEMIS Mission, specifically the ESA, EFI, and FGM teams. Work at MIT Haystack Observatory was supported by NSF Cooperative Agreement AGS-1242204.

## Supplementary Materials

www.sciencemag.org/content/343/6175/1122/suppl/DC1
Supplementary Text
Table S1
References (*23*–*26*)

15 October 2013; accepted 6 February 2014
10.1126/science.1247212



# Tunable Phonon Polaritons in Atomically Thin van der Waals Crystals of Boron Nitride

S. Dai,[1] Z. Fei,[1] Q. Ma,[2] A. S. Rodin,[3] M. Wagner,[1] A. S. McLeod,[1] M. K. Liu,[1] W. Gannett,[4,5] W. Regan,[4,5] K. Watanabe,[6] T. Taniguchi,[6] M. Thiemens,[7] G. Dominguez,[7,8] A. H. Castro Neto,[3,9] A. Zettl,[4,5,10] F. Keilmann,[11] P. Jarillo-Herrero,[2] M. M. Fogler,[1] D. N. Basov[1]*

van der Waals heterostructures assembled from atomically thin crystalline layers of diverse two-dimensional solids are emerging as a new paradigm in the physics of materials. We used infrared nanoimaging to study the properties of surface phonon polaritons in a representative van der Waals crystal, hexagonal boron nitride. We launched, detected, and imaged the polaritonic waves in real space and altered their wavelength by varying the number of crystal layers in our specimens. The measured dispersion of polaritonic waves was shown to be governed by the crystal thickness according to a scaling law that persists down to a few atomic layers. Our results are likely to hold true in other polar van der Waals crystals and may lead to new functionalities.

Layered van der Waals (vdW) crystals consist of individual atomic planes weakly coupled by vdW interaction, similar to graphene monolayers in bulk graphite (*1*–*3*). These materials can harbor superconductivity (*2*) and ferromagnetism (*4*) with high transition

temperatures, emit light (*5*, *6*), and exhibit topologically protected surface states (*7*), among many other effects (*8*). An ambitious practical goal (*9*) is to exploit atomic planes of vdW crystals as building blocks of more complex artificially stacked structures where each such block will deliver layer-specific attributes for the purpose of their combined functionality (*3*). We explored the behavior of phonon polaritons in hexagonal boron nitride (hBN), a representative vdW crystal. The phonon polaritons are collective modes that originate from coupling of photons with optical phonons (*10*) in polar crystals. They have been investigated in the context of energy transfer (*11*, *12*), coherent control of the lattice (*13*), ultramicroscopy (*14*, *15*), "superlensing" (*16*), and metamaterials (*17*, *18*). Tunable phonon polaritons that we discovered in hBN by direct infrared (IR) nanoimaging set the stage for the implementation of these appealing concepts in vdW heterostructures. Polaritonic effects reported here are likely generic to other polar vdW solids because these materials commonly show optical phonons. hBN stands out in this class of materials thanks to its light constituent elements, which yield particularly strong phonon resonances that span a broad region of the technologically important IR band.

IR nanoimaging and Fourier transform IR nano-spectroscopy (nano-FTIR) experiments were performed at UCSD by using a scattering-type scanning near-field optical microscope (s-SNOM) (*19*). The physics of polariton imaging using s-SNOM is akin to nanoimaging of surface plasmons (*20*, *21*) (Fig. 1A). In short, we illuminated the metalized tip of an atomic force microscope (AFM) with an IR beam. We used quantum cascade lasers (QCLs) with tunable frequency $\omega = 1/\lambda_{IR}$, where $\lambda_{IR}$ is IR beam wavelength and a broad-band difference frequency generation (DFG) laser system (*22*). Our AFM tip with curvature radius $a \approx 25$ nm is polarized by the incident IR beam. The light momenta imparted by the tip extend to the typical range of momenta supporting phonon polaritons in hBN (Fig. 2E). Therefore, the strong electric field between the tip and the sample provides the necessary momentum to launch polariton waves of wavelength $\lambda_p$ that propagate radially outward from the tip along the hBN surface. AFM tips exploited in our nanospectroscopy instrument are commonly referred to as optical antennas (*23*): an analogy that is particularly relevant to describe the surface wave launching function of the tip. Upon reaching the sample edge, polaritonic waves are reflected back, forming a standing wave between the tip and hBN edge. As the tip is scanned toward the edge, the scattering signal collected from underneath the tip reveals oscillations with the period of $\lambda_p/2$.

Representative nanoimaging data are displayed in Fig. 1, B and D to F, where we plot the normalized near-field amplitude $s(\omega) = s_{hBN}(\omega)/s_{Au}(\omega)$ at several IR frequencies in the 1550- to 1580-$cm^{-1}$ range. Here, $s_{hBN}(\omega)$ and $s_{Au}(\omega)$ are the scattering amplitudes for, respectively, the sample and the reference (Au-coated wafer) (*19*). The amplitudes were demodulated at the third or the fourth harmonic of the tapping frequency to isolate the genuine near-field signal (*23*). The images in Fig. 1, B to F, were taken for a tapered hBN crystal of thickness $d = 256$ nm. They reveal a hatched pattern of periodic maxima, fringes, of $s(\omega)$ running parallel to the edges, with the "hot spots" located where two or more fringes intersect. We observed similar fringe patterns in other hBN samples, including those that are only a few atomic layers thick (Fig. 1G). Such patterns are readily accounted for (Fig. 1C) within a phenomenological theory that considers reflections from the tapered edges (*19*).

Data in Fig. 1 allow one to obtain the polariton wavelength $\lambda_p$ simply by doubling the fringe period, and the corresponding momentum can be calculated as $q = 2\pi/\lambda_p$. We used two approaches to determine the dispersion relation $q = q(\omega)$ of the polaritons. One method (*15*, *20*, *21*) is to analyze the periodicity of fringes at discrete frequencies of the IR source (Fig. 1, B and D to G). We have complemented this procedure with a technique capable of capturing the entire dispersion in the course of one single scan of our nanoscope. We executed this line scan on an hBN crystal with a large surface area to ensure that the $L = 0$ boundary is the principal reflector for the tip-launched polaritons (Fig. 2A). Such a line scan (Fig. 2, A, B, and D) is composed of a series of broad-band nano-FTIR spectra taken at every pixel. Starting in the region of unobscured $SiO_2$ substrate ($L < 0$) and continuing through the hBN crystal ($L > 0$), we combined the spectra from all pixels along the line scan and thus obtained a two-dimensional map $s(L, \omega)$, shown in Fig. 2B. In the plot, we observed a series of resonances that systematically vary with frequency ω and the distance from the sample edge

[1]Department of Physics, University of California, San Diego (UCSD), La Jolla, CA 92093, USA. [2]Department of Physics, Massachusetts Institute of Technology, Cambridge, MA 02139, USA. [3]Department of Physics, Boston University, Boston, MA 02215, USA. [4]Department of Physics, University of California, Berkeley, Berkeley, CA 94720, USA. [5]Materials Sciences Division, Lawrence Berkeley National Laboratory, Berkeley, CA 94720, USA. [6]National Institute for Materials Science, Namiki 1-1, Tsukuba, Ibaraki 305-0044, Japan [7]Department of Chemistry and Biochemistry, University of California, San Diego, La Jolla, CA 92093, USA. [8]Department of Physics, California State University, San Marcos, San Marcos, CA 92096, USA. [9]Graphene Research Centre and Physics Department, National University of Singapore, 6 Science Drive 2, Singapore 117546, Singapore. [10]Kavli Energy NanoSciences Institute at the University of California, Berkeley, and the Lawrence Berkeley National Laboratory, Berkeley, CA 94720, USA. [11]Ludwig-Maximilians-Universität and Center for Nanoscience, 80539 München, Germany.

*Corresponding author. E-mail: dbasov@physics.ucsd.edu

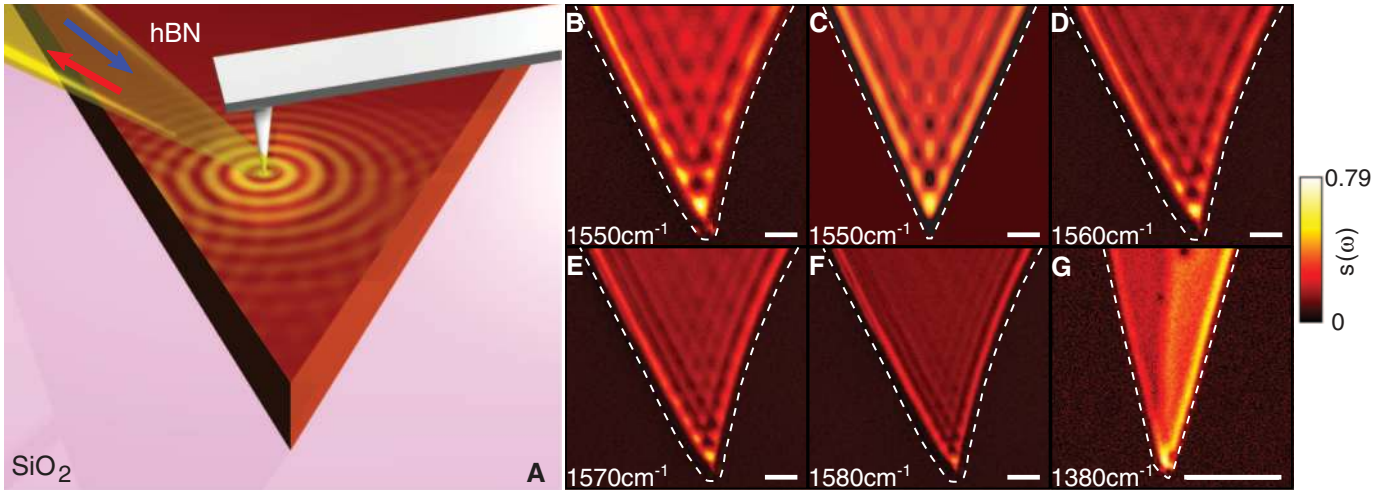


**Fig. 1. Real-space imaging of surface phonon polaritons on hBN.** (**A**) Schematics. Arrows denote the incident and back-scattered IR light. Concentric yellow circles illustrate the phonon polariton waves launched by the AFM tip and reflected by the two edges of a tapered hBN crystal. (**B** and **D** to **F**) IR near-field images of the normalized amplitude $s(\omega)$ defined in the text and taken at different IR frequencies [hBN thickness in (B) to (F) $d = 256$ nm]. (**C**) Simulation of the phonon polariton interference pattern (*19*). (**G**) Phonon polaritons probed in three-layer (left) and four-layer (right) hBN crystals. White dashed line tracks the hBN edges according to the AFM topography. Scale bars indicate 800 nm.

$L$. The nano-FTIR spectra from three representative positions are shown in Fig. 2C. Each of the frames in Fig. 2C and each pixel in Fig. 2B unveil phonon polaritons in the frequency domain. The momentum $q$ corresponding to each $\omega$ in this map can be found from the fringe periodicity along the $\omega$ = constant cut. Therefore, a single line scan is sufficient to extract the complete dispersion profile of any surface mode.

The two approaches for mapping the surface wave dispersion produced consistent results (triangles in Fig. 2B were obtained from monochromic imaging). The broad-band line scan data (dots in Fig. 2E) allowed us to probe the dispersion in the $\omega - q$ parameter space (1430 to 1530 $cm^{-1}$) that cannot be investigated through the single-frequency imaging because of unavailability of proper QCLs. The experimental data for phonon polariton dispersion in Fig. 2E are in excellent agreement with the modeling results. Briefly, the surface polaritons correspond to the divergences of the reflectivity $r_p(q + i\kappa, \omega)$ of the system at complex momenta $q + i\kappa$ (*10*). For $\lambda_p \ll \lambda_{IR}$, we derived the analytical formula for polariton dispersion (*19*):

$$q(\omega) + i\kappa(\omega) = -\frac{\psi}{d}\left[\arctan\left(\frac{\varepsilon_a}{\varepsilon_\perp \psi}\right) + \arctan\left(\frac{\varepsilon_s}{\varepsilon_\perp \psi}\right) + \pi l\right], \quad \psi = \frac{\sqrt{\varepsilon_\parallel}}{i\sqrt{\varepsilon_\perp}} \qquad (1)$$

where $\varepsilon_a(\omega)$, $\varepsilon_\perp(\omega)$, $\varepsilon_\parallel(\omega)$, and $\varepsilon_s(\omega)$ are the dielectric functions of air, hBN (for directions perpendicular and parallel to the $c$ axis), and $SiO_2$ substrate, respectively. The propagating modes correspond only to those integer $l$ (if any) for which the loss factor $\gamma = \alpha\kappa/q$ is positive and less than unity. Parameter $\alpha = \pm$ is the sign of the group velocity $d\omega/dq$ (*19*). An instructive way to visualize both the dispersion and the damping is via a false-color plot of Im $r_p(q, \omega)$ (*19*, *24*) at real $q$ and $\omega$ (Fig. 2E). Our data line up with the topmost of these curves, which corresponds to the principal $l = 0$ branch (*19*) in Eq. 1.

Additional insights into the photonic and polaritonic properties of hBN were obtained by analyzing the frequency dependence of the nano-FTIR spectra. We collected the spectrum in Fig. 2F far away from the hBN edges, where the surface waves are damped and the scattering amplitude signal is solely governed by the

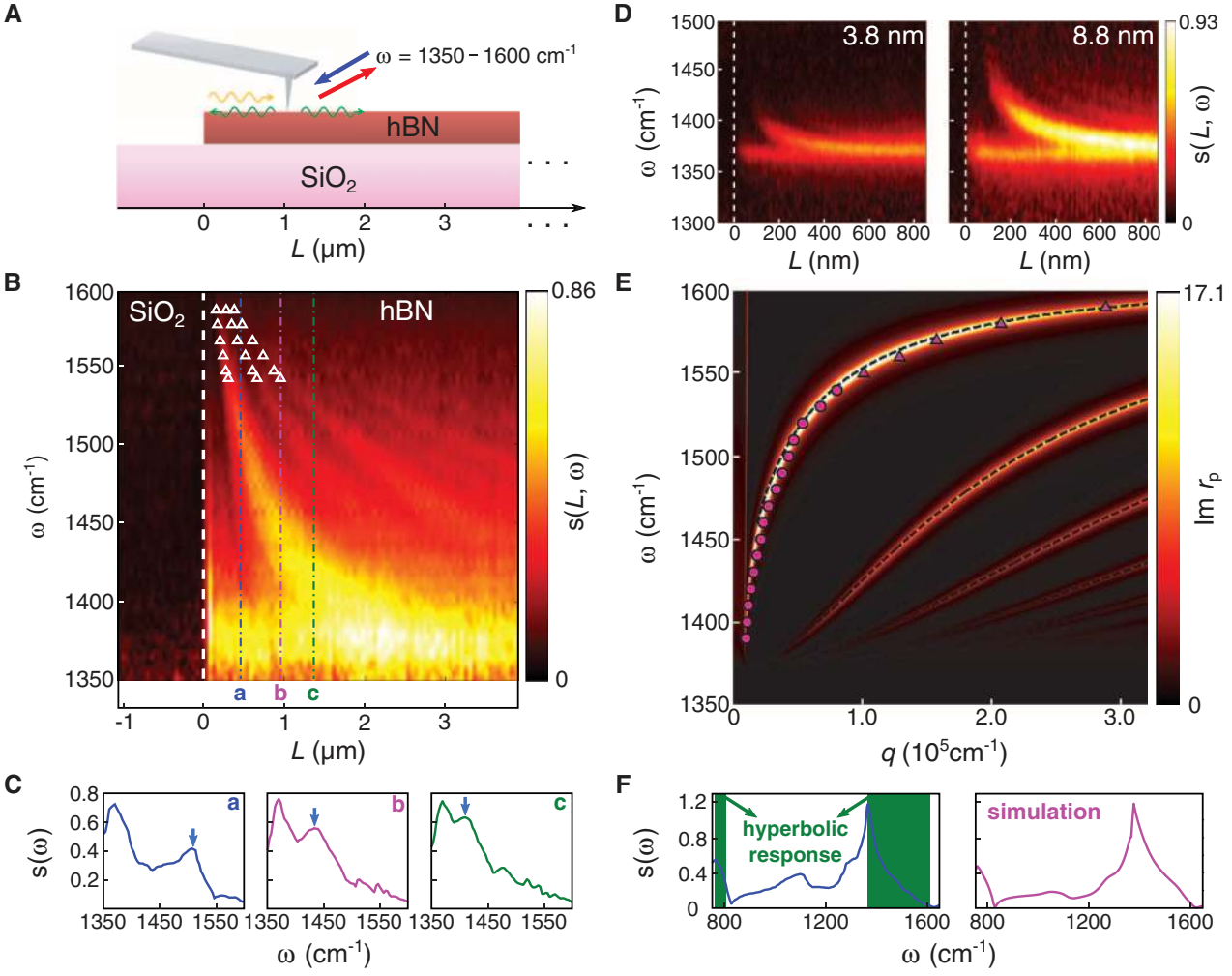


**Fig. 2. The surface phonon polariton dispersion and nano-FTIR spectra. (A)** Schematics of a nano-FTIR line scan across the hBN crystal. Arrows denote the incident and back-scattered IR beam spanning 1350 to 1600 $cm^{-1}$. Polaritonic waves are launched (green) by AFM tip and then reflected (orange) by hBN edge at $L = 0$. **(B)** Polaritonic features detected in a single line scan in (A). The normalized scattering amplitude spectra $s(\omega)$ is plotted in the false color scale. White dashed line at $L = 0$ marks the edge of the hBN crystal (thickness $d = 134$ nm). Triangles, fringe maxima extracted from monochromatic imaging similar to Fig. 1. **(C)** Nano-FTIR spectra at three representative locations along the line scan marked in (B). The peaks marked by the arrows correspond to the dominant polariton interference fringe. **(D)** Phonon polariton features as probed via line scans for ultrathin hBN crystals with $d = 3.8$ nm (left) and $d = 8.8$ nm (right). **(E)** The dispersion relation of phonon polaritons in hBN. Triangles indicate data from monochromatic imaging in Fig. 1; dots, the nano-FTIR results from (B). The data are superimposed on a false-color plot of calculated Im $r_p$ (*19*); the black dashed lines are from Eq. 1. The straight line on the left represents the light line. **(F)** Nano-FTIR spectrum $s(\omega)$ for the hBN crystal (Fig. 1, A to F) taken away from the sample edges. The solid (green) part of the data corresponds to hBN's hyperbolic region where $\mathrm{Re}\varepsilon_\perp \cdot \mathrm{Re}\varepsilon_\parallel < 0$.

local interaction with the phonon resonances (*25*). Two of these resonances centered around 770 and 1370 $cm^{-1}$ are due to the *c* axis and the in-plane phonon modes of hBN, respectively (*26*, *27*). The hump-dip feature around 1100 $cm^{-1}$ originates from the $SiO_2$ substrate (*28*): a consequence of a partial transparency of our specimen. The quantitative relation between this spectrum, the reflectivity $r_p(q, \omega)$, and the fundamental phonon modes can be established by numerical modeling of the tip-sample interaction (*19*). The right plot of Fig. 2F indicates that our model captures the gross features of the data. Moreover, the hBN is an example of a natural hyperbolic material (*29*): a crystal possessing the in-plane and out-of-plane components of the dielectric tensor having the opposite signs so that $\mathrm{Re}\varepsilon_\perp \cdot \mathrm{Re}\varepsilon_\parallel < 0$. Hyperbolic regions are marked in green in Fig. 2F.

The layered nature of vdW materials, including hBN, facilitates the control of both the wavelength and the amplitude of polaritonic waves by varying the thickness *d* of the specimens. Representative line profiles (Fig. 3A) for specimens with *d* in the range of 150 to 250 nm were taken normal to the crystal edge at $L = 0$. The thickness was measured simultaneously with the scattering amplitude through the AFM topography. All fringe profiles share the same line form with a prominent peak close to the edge followed by weaker peaks that are gradually suppressed away from the edge. The oscillation period, equal to $\lambda_p/2$ (arrows in Fig. 3A), systematically decreases as the samples become thinner. This scaling extends down to a few atomic layers (Fig. 3, B and C).

The measured polariton wavelength (Fig. 3E) agrees with the theoretical predictions (Fig. 3D). For $\lambda_p$ smaller than about one-half of $\lambda_{IR} = 7.1$ μm, the polariton wavelength scales linearly with the crystal thickness *d*, in agreement with Eq. 1; at larger $\lambda_p$, the linear law shows signs of saturation, also in accord with our model (Fig. 3E inset). Experimentally, the phonon polaritons display thickness-tunability persisting down to three atomic layers (Fig. 3, B and C). We detected polaritons in even thinner samples (bilayer and monolayer hBN). However, the quantitative analysis of these latter data is complicated because of the increasing role of the substrate in the polaritonic response that calls for further experiments on suspended membranes.

Similar to surface plasmons, the phonon polaritons allow one to confine and control electromagnetic energy at the nanoscale (*30*). In fact, the line form in Fig. 3A strongly resembles plasmonic standing waves in graphene (*20*, *21*). The confinement factor $\lambda_{IR}/\lambda_p$ reaches 25 in hBN, comparable to that of plasmons in graphene (*20*, *21*). Yet these compact polaritons in hBN are able to travel at least 5 to 10 μm, compared with less than 0.5 μm for graphene plasmons. The corresponding loss factor $\gamma = \alpha\kappa/q$ is around 0.055, much smaller than a typical γ in graphene. The low damping of polaritons in our insulating samples is consistent with the absence of the electronic losses, the dominant damping channel in plasmonics. The observed losses can likely be further suppressed by improving the crystallographic order of the crystals.

Data in Figs. 1 to 3 show that phonon polaritons of the desired wavelength and confinement can be engineered by varying the number of atomic layers in hBN by, for example, exfoliation techniques. Thus, hBN and likely other polar layered materials can be integrated into vdW hetrostructures (*3*) to serve not only as electrically insulating spacers but also as waveguides for weakly damped polaritons capable of traveling over considerable distances. Additionally, the hyperbolic response of few-layer hBN is appealing in the context of unique nanophotonics characteristics of this class of solids (*29*).



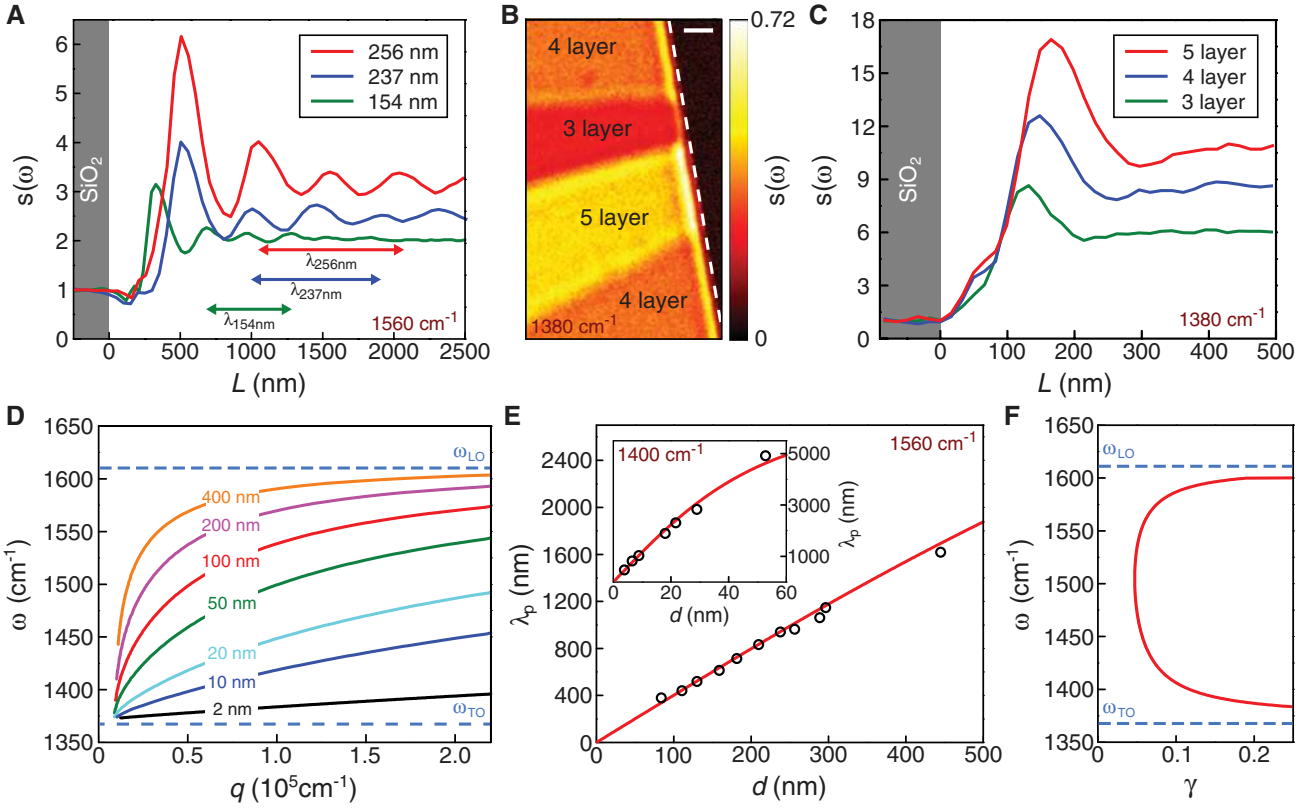


**Fig. 3. The evolution of the phonon polariton wavelength and amplitude with the thickness of hBN crystals.** (**A**) Line profiles of the scattering amplitude $s(\omega)$ at 1560 $cm^{-1}$ for hBN crystals with $d = 154$, 237, and 256 nm. Arrows indicate the polariton wavelength. (**B**) Near-field image and (**C**) phonon polariton line profiles for few-layer hBN crystals. White dashed line in (B) tracks the sample boundary; scale bar in (B), 400 nm. (**D**) Calculated dispersion relation of the $l = 0$ branch of the phonon polaritons in hBN for various crystal thicknesses (*d*). TO and LO frequencies are marked with blue dashed lines. (**E**) Dots, wavelengths of phonon polaritons probed at 1560 $cm^{-1}$ for crystals with different thicknesses (*d*); red line, calculated thickness-dependence relation. (Inset) Thickness-dependence relation probed at 1400 $cm^{-1}$ for ultrathin hBN crystals. See (*19*) for details. (**F**) Calculated loss factor for phonon polaritons.

**References and Notes**

1. C. R. Dean *et al.*, *Nat. Nanotechnol.* **5**, 722–726 (2010).
2. K. S. Novoselov *et al.*, *Proc. Natl. Acad. Sci. U.S.A.* **102**, 10451–10453 (2005).
3. A. K. Geim, I. V. Grigorieva, *Nature* **499**, 419–425 (2013).
4. T. Kimura, Y. Tokura, *Annu. Rev. Mater. Sci.* **30**, 451–474 (2000).
5. K. F. Mak, C. Lee, J. Hone, J. Shan, T. F. Heinz, *Phys. Rev. Lett.* **105**, 136805 (2010).
6. A. Splendiani *et al.*, *Nano Lett.* **10**, 1271–1275 (2010).
7. X. Qi, S. Zhang, *Rev. Mod. Phys.* **83**, 1057–1110 (2011).
8. L. Britnell *et al.*, *Science* **340**, 1311–1314 (2013).
9. S. Z. Butler *et al.*, *ACS Nano* **7**, 2898–2926 (2013).
10. L. Novotny, B. Hecht, *Principles of Nano-Optics* (Cambridge Univ. Press, Cambridge, 2006).
11. J. Renger, S. Grafström, L. M. Eng, R. Hillenbrand, *Phys. Rev. B* **71**, 075410 (2005).
12. S. Shen, A. Narayanaswamy, G. Chen, *Nano Lett.* **9**, 2909–2913 (2009).
13. T. Feurer, J. C. Vaughan, K. A. Nelson, *Science* **299**, 374–377 (2003).
14. Y. De Wilde *et al.*, *Nature* **444**, 740–743 (2006).
15. A. Huber, N. Ocelic, D. Kazantsev, R. Hillenbrand, *Appl. Phys. Lett.* **87**, 081103 (2005).
16. T. Taubner, D. Korobkin, Y. Urzhumov, G. Shvets, R. Hillenbrand, *Science* **313**, 1595 (2006).
17. G. Shvets, *Phys. Rev. B* **67**, 035109 (2003).
18. J. A. Schuller, R. Zia, T. Taubner, M. L. Brongersma, *Phys. Rev. Lett.* **99**, 107401 (2007).
19. Materials and methods are available as supplementary materials on *Science* Online.
20. J. Chen *et al.*, *Nature* **487**, 77–81 (2012).
21. Z. Fei *et al.*, *Nature* **487**, 82–85 (2012).
22. F. Keilmann, S. Amarie, *J. Infrared Millimeter Terahertz Waves* **33**, 479–484 (2012).
23. J. M. Atkin, S. Berweger, A. C. Jones, M. B. Raschke, *Adv. Phys.* **61**, 745–842 (2012).
24. Z. Fei *et al.*, *Nano Lett.* **11**, 4701–4705 (2011).
25. R. Hillenbrand, T. Taubner, F. Keilmann, *Nature* **418**, 159–162 (2002).
26. R. Geick, C. H. Perry, G. Rupprecht, *Phys. Rev.* **146**, 543–547 (1966).
27. X. G. Xu, A. E. Tanur, G. C. Walker, *J. Phys. Chem. A* **117**, 3348–3354 (2013).
28. L. M. Zhang *et al.*, *Phys. Rev. B* **85**, 075419 (2012).
29. A. Poddubny, I. Iorsh, P. Belov, Y. Kivshar, *Nat. Photonics* **7**, 948–957 (2013).
30. R. Stanley, *Nat. Photonics* **6**, 409–411 (2012).



**Acknowledgments:** Work at UCSD was supported by U.S. Department of Energy–Office of Basic Energy Sciences (DOE-BES). The development of nano-FTIR at UCSD is supported by Office of Naval Research (ONR), DOE, Air Force Office of Scientific Research (AFOSR), and NSF. M.M.F. is supported by ONR. P.J.-H. acknowledges support from AFOSR grant number FA9550-11-1-0225. A.S.R. acknowledges DOE grant DE-FG02-08ER46512 and ONR grant MURI N00014-09-1-1063. M.T. and G.D. are supported by NASA. A.H.C.N. acknowledges a National Research Foundation–Competitive Research Programme award (R-144-000-295-281). A.Z., W.G., and W.R. acknowledge support from the Director, Office of Energy Research, BES, Materials Sciences and Engineering Division, of the U.S. DOE under contract no. DE-AC02- 05CH11231, which provided for preparation and characterization of the BN, and from the ONR, which provided for substrate transfer technique. F.K. is a cofounder of Neaspec, producer of the s-SNOM apparatus used in this study.


**Supplementary Materials**

www.sciencemag.org/content/343/6175/1125/suppl/DC1
Materials and Methods
Supplementary Text
Figs. S1 to S5
References (*31*–*42*)


4 October 2013; accepted 6 February 2014
10.1126/science.1246833


# Rapid Reductions in North Atlantic Deep Water During the Peak of the Last Interglacial Period


**Eirik Vinje Galaasen,[1]* Ulysses S. Ninnemann,[1,2] Nil Irvalı,[2] Helga (Kikki) F. Kleiven,[1,2] Yair Rosenthal,[3] Catherine Kissel,[4] David A. Hodell[5]**



Deep ocean circulation has been considered relatively stable during interglacial periods, yet little is known about its behavior on submillennial time scales. Using a subcentennially resolved epibenthic foraminiferal $\delta^{13}C$ record, we show that the influence of North Atlantic Deep Water (NADW) was strong at the onset of the last interglacial period and was then interrupted by several prominent centennial-scale reductions. These NADW transients occurred during periods of increased ice rafting and southward expansions of polar water influence, suggesting that a buoyancy threshold for convective instability was triggered by freshwater and circum-Arctic cryosphere changes. The deep Atlantic chemical changes were similar in magnitude to those associated with glaciations, implying that the canonical view of a relatively stable interglacial circulation may not hold for conditions warmer and fresher than at present.


Future climate could be affected on a global scale if the circulation of North Atlantic Deep Water (NADW), the main water mass ventilating the deep Atlantic (Fig. 1) (*1*), is altered. Such changes could have widespread and long-lasting impacts—including, for example, on regional sea level (*2*), the intensity and pacing of Sahel droughts (*3*), and the pattern and rate of ocean acidification and $CO_2$ sequestration (*4*). However, the response of NADW to high-latitude warming and ocean freshening, both of which would decrease source region density and potentially inhibit NADW formation, remains a key uncertainty in future climate projections. Model estimates range from nearly no change to ~50% reduction in Atlantic Meridional Overturning Circulation by 2100 CE (*5*). Compounding the uncertainty, models may inherently underestimate the possibility for abrupt and large changes (*6*), and there may even be critical stability thresholds in surface ocean buoyancy that, if crossed, could switch circulation into an equilibrium state without strong NADW formation (*7*, *8*). The current consensus is that we are far from any such stability thresholds and that the modern style of vigorous NADW ventilation is a robust feature of warm interglacial climates. Only modest millennial-scale NADW variability has been found to occur during interglacials (*9*, *10*) relative to that seen during colder glacial periods (*11*). However, large but shorter-lived transient anomalies might be possible even in the midst of a generally vigorous interglacial circulation (*7*, *12*, *13*). Hence, reconstructions with appropriate resolution to characterize the short-term instability of NADW during warmer climates are needed to assess model fidelity and constrain possible tipping points for ocean circulation. We used deep sea sediment proxy records from key locations (Fig. 1) to assess the occurrence and magnitude of centennial-scale variability in NADW over the warm interval of the last interglacial period (LIG) [marine isotope stage (MIS) 5e]. The LIG is a useful period for evaluating the sensitivity of NADW to key features that we may face in the future, including a warmer and fresher North Atlantic than at present (*14*, *15*) and the retreat of the circum–North Atlantic cryosphere (*15*, *16*).

We characterized the short-term variability of NADW over the LIG using sediment core MD03-2664 (57°26.34′N, 48°36.35′W; 3442 m water depth) from the Eirik Drift site used to identify the centennial-scale NADW reduction associated with the climate anomaly 8.2 thousand years before the present (ky B.P.) (*12*). This site monitors the newly formed, integrated Nordic Seas overflows (*12*) that are the primary constituents of lower NADW (*1*). The high sedimentation rate (~35 cm $ky^{-1}$) at this location allows a multidecadal depiction of lower NADW properties and ventilation across the LIG (~30 years per 1-cm sample), which is approximately an order of magnitude greater than the previous reconstructions used to infer millennial-scale NADW stability during the LIG (*10*, *17*).

On our age model (*18*), the MIS 5e "plateau" [the interval of relatively constant minimum ice volume (benthic $\delta^{18}O$)] corresponds to 116.1 to 128.0 ky. We focused our study on this interval, referring to it as the LIG. We documented NADW variability using the carbon isotopic composition


[1]Department of Earth Science, University of Bergen and Bjerknes Centre for Climate Research, Allégaten 41, 5007 Bergen, Norway. [2]Uni Climate, Uni Research and Bjerknes Centre for Climate Research, Bergen, Norway. [3]Institute of Marine and Coastal Sciences and Department of Earth and Planetary Sciences, Rutgers University, New Brunswick, NJ, USA. [4]Laboratorie des Sciences du Climat et de l'Environnement/Institut Pierre Simon Laplace, CEA/CNRS/UVSQ, Gif-sur-Yvette, France. [5]Godwin Laboratory for Paleoclimate Research, Department of Earth Sciences, University of Cambridge, Cambridge, UK.

*Corresponding author. E-mail: eirik.galaasen@geo.uib.no

Science

# Tunable Phonon Polaritons in Atomically Thin van der Waals Crystals of Boron Nitride

S. Dai, Z. Fei, Q. Ma, A. S. Rodin, M. Wagner, A. S. McLeod, M. K. Liu, W. Gannett, W. Regan, K. Watanabe, T. Taniguchi, M. Thiemens, G. Dominguez, A. H. Castro Neto, A. Zettl, F. Keilmann, P. Jarillo-Herrero, M. M. Fogler and D. N. Basov

*Science* **343** (6175), 1125-1129.
DOI: 10.1126/science.1246833

**Nanoimaged Polaritons**

Engineered heterostructures consisting of thin, weakly bound layers can exhibit many attractive electronic properties. **Dai *et al.*** (p. 1125) used infrared nanoimaging on the surface of hexagonal boron nitride crystals to detect phonon polaritons, collective modes that originate in the coupling of photons to optical phonons. The findings reveal the dependence of the polariton wavelength and dispersion on the thickness of the material down to just a few atomic layers.

www.sciencemag.org/content/343/6175/1125/suppl/DC1

# Supplementary Materials for

## Tunable Phonon Polaritons in Atomically Thin van der Waals Crystals of Boron Nitride

S. Dai, Z. Fei, Q. Ma, A. S. Rodin, M. Wagner, A. S. McLeod, M. K. Liu, W. Gannett, W. Regan, K. Watanabe, T. Taniguchi, M. Thiemens, G. Dominguez, A. H. Castro Neto, A. Zettl, F. Keilmann, P. Jarillo-Herrero, M. M. Fogler, D. N. Basov*

*Corresponding author. E-mail: dbasov@physics.ucsd.edu

Published 7 March 2014, *Science* **343**, 1125 (2014)
DOI: 10.1126/science.1246833

**This PDF file includes:**

## Materials and Methods

Preparation and characterization of hBN crystals

Microcrystals of hBN were exfoliated from bulk samples and then transferred to Si wafers capped with 300 nm-thick $SiO_2$ layer. We explored bulk hBN samples from two different sources including commercially available samples (www.momentive.com) and also specimens synthesized by means of high pressure techniques as described in Ref. (*31*). We observed reproducible polaritonic effects irrespective of the origin of our microcrystals. Raman spectroscopy was applied to characterize the hBN crystals. (Fig. S1B). These Raman spectra were in accord with the literature data for high-quality hBN specimens (*32*). We note that one can easily distinguish hBN crystals of different thickness by their color under the optical microscope (Fig. S1A) (*33*).

Infrared nano-imaging and nano-FTIR

The nano-imaging and Fourier transform infrared nano-spectroscopy (nano-FTIR) data were obtained using a commercial scattering-type scanning near-field optical microscope (s-SNOM) (www.neaspec.com) based on a tapping-mode atomic force microscope (AFM). The tapping frequency and amplitude of the AFM are about 250 *kHz* and 70 nm, respectively. In Fig. S2, we show schematics of our infrared (IR) sources and of the s-SNOM system. These IR sources include tunable quantum cascade lasers (QCLs) (www.daylightsolutions.com) and a broad-band source based on a difference frequency generation (DFG) system (www.lasnix.com). In combination, these sources cover a broad frequency range from 700 to 2300 $cm^{-1}$ (Fig. S2). By focusing the IR beam onto the metalized AFM tip, we were able to probe the polaritonic effects of hBN. The back-scattered signal by the tip is registered by pseudoheterodyne interferometric detection and then demodulated at the $n$-th harmonics of the tapping frequency yielding background free images. In this work, we chose $n = 3$ or 4.

## Supplementary Text

Modeling near field spectra and images due to phonon polariton waves in hBN

1. Tip-launched surface waves

We start with describing a model that captures the essence of the observed real-space patterns in Figs. 1−3 on purely phenomenological grounds. This model assumes that the near-field contrast detected by the s-SNOM is in the linear response regime and is purely local. In other words, the deviation of the s-SNOM signal from the area average is given by some linear functional $E(\mathbf{r})$ of the electric potential $\phi(\boldsymbol{r})$ directly underneath the tip. The qualitative aspects of the results do not depend on the precise relation between $\phi(\boldsymbol{r})$ and $E(\boldsymbol{r})$ as long as this relation is linear. For definiteness, one can think that $E(\mathbf{r})$ represents the deviation of the $z$-component of the local electric field from its average value, so we use the term "field" to refer to it from now on. We

further assume that tip-launched polaritons are characterized by the radially symmetric field distribution ($r = |\boldsymbol{r}|$)

$$E(r) = E_0 e^{iqr} \times \begin{cases} e^{-r^2/4r_0^2}, & r < r_0 \\ e^{-1/4}(r_0/r)^{1/2}, & r \geq r_0 \end{cases}, \tag{S1}$$

where we take $r_0 = \lambda_p/4$ (the diffraction limit), $\lambda_p$ is the phonon polariton wavelength. Eq. S1 is designed to have the property that $E(r)$ goes to a constant underneath the tip ($r \to 0$) and behaves as an outgoing cylindrical wave at large distances. The momentum of this wave is a complex number

$$q_p = q + i\kappa = q(1 + i\gamma) = \frac{2\pi}{\lambda_p}(1 + i\gamma), \tag{S2}$$

where $\gamma = \kappa / q$ is the loss factor defined in the main text.

2. Near-field images of phonon polaritons

The observed polariton interference fringes (Figs. 1−3) originate from the superposition of tip-launched polariton waves with those reflected back from the edges of the hBN crystals. The edge-reflected waves can be approximately calculated using the method of images. For a single edge (Fig. S3A), the total field under the tip (solid red arrow) is given by $E_{\text{tot}} = E(0) + E(2L)r_{sp}$, where $L$ is the tip-edge distance, $r_{sp}$ is the complex coefficient of reflection off the edge, and function $E(r)$ is given by Eq. S1.

For the tapered hBN crystal (Fig. 1), the polariton waves launched by the tip may experience multiple reflections. Therefore, we introduce the index $m = 1, 2, \ldots$ to label the waves that are reflected $m$ times by the edges before arriving back to the tip; we refer to them as the $m$-th order waves. The locations of the corresponding image sources are obtained by $m$ consecutive mirror reflections of the tip across the alternate edges. We refer to them as the $m$-th order images. In Fig. S3B we show these multiple tip images (hollow dots) for one representative tip position (solid green dot). We use the double index "$m,n$" to label the $n$-th ($n = 1$ or 2) possible position of the $m$-th order images. Let $d_{m,n}$ be the distance between the $n$-th position of the $m$-th order images and the tip. The total polaritonic field underneath the tip can be expressed as:

$$E_{\text{tot}} = \sum_m \sum_n E(d_{m,n}) r_{sp}^m . \tag{S3}$$

Using this formula we computed $E_{\text{tot}}$ for every position within a triangular area representing the tapered hBN crystal in Fig. 1 of the main text. For this particular sample geometry only $m \leqslant 3$ images contribute to the formation of the interference patterns in the field of view.

Our simulation results are shown in Fig. 1C of the main text. We find a good qualitative agreement with the actual data (Fig. 1B) using the parameters $\gamma = 0.055$ and $r_{sp} = -0.2 + 0.3i$, which are in accord with the phonon polariton line profiles (Fig. 3A). Simulation images for the different choices of $\gamma$ value along with the experimental data are shown in Fig. S4. The fact that the absolute value of $r_{sp}$ is smaller than unity suggests that either the reflection has a strong diffuse component or a significant amount of energy is dissipated into degrees of freedom other than the principal polariton branch ($l = 0$ in the main text). Among the dominant factors reducing the reflectivity of polaritons are the roughness as well as canted nature of the edges.

Besides analyzing the two-dimensional interference patterns, we also examined the line profiles (Fig. 3A). Noticing a marked resemblance between the observed phonon polariton

fringes and the plasmonic interference fringes in graphene (*20*, *21*), we attempted to roughly estimate the former using the simulation developed previously for the latter. In this way, we again arrived at the estimated range $\gamma \approx 0.04-0.07$.

3. Optical constants and infrared reflectivity of hBN

The infrared reflectivity of boron nitride (BN) has been investigated by several groups (*26*, *34-36*). A consensus is that both the in-plane and the out-of-plane dielectric function can each be described by a single Lorentzian:

$$\varepsilon_\mu = \varepsilon_{\infty\mu} + \varepsilon_{\infty\mu} \frac{(\omega_{LO,\mu})^2 - (\omega_{TO,\mu})^2}{(\omega_{TO,\mu})^2 - \omega^2 - i\omega\Gamma_\mu}, \quad \mu = \perp, //, \tag{S4}$$

with nearly the same values of the optical phonon frequencies $\omega_{TO,\mu}$ and $\omega_{LO,\mu}$ reported by all the groups. These values are also in a good agreement with the results of *ab initio* calculations (*37*, *38*). However, we met some difficulty finding reliable experimental data in the literature for limiting high-frequency values $\varepsilon_{\infty\mu}$ and especially the optical phonon broadening $\Gamma_\mu$. The aforementioned experiments studied boron nitride samples obtained by pyrolysis (*26*), chemical-vapor-deposition (CVD) (*34*), and magnetron sputtering (*35*, *36*). All of these materials were composed of misoriented (angle spread $\theta \sim \pm 30^0$) grains of sub-10 nm size. For such small grain sizes, the linewidth broadening of the phonons can be considerably larger than what is expected in single-crystals, as was shown by Raman studies (*39*, *40*). On the other hand, $\Gamma_\mu$ as small as a few $cm^{-1}$ was estimated for the CVD-grown rhombohedral boron nitride. This material has the same in-plane layer structure and nearly the same phonon frequencies as CVD hBN but a much higher degree of crystallographic order (*34*). For all of the above reasons, in our calculations we used the parameters of Cai *et al.* (*37*) with the broadening $\Gamma_{//} = 4$ $cm^{-1}$ and $\Gamma_\perp = 5$ $cm^{-1}$ in order to reproduce the observed loss factor $\gamma \approx 0.055$ at 1550$cm^{-1}$ (see Fig. 3F of the main text).

The dielectric function of Eq. S4 serves as input into the calculation of the complex reflectivity $r_p(q, \omega)$ and therefore of the phonon polariton dispersion. Although our system consisted of three layers: hBN, $SiO_2$, and Si, at large $q$ relevant for our experiments, the electric field of the polaritons is mostly confined in the first two layers. Therefore, it is legitimate to approximate $r_p(q, \omega)$ by the reflectivity of a simpler hBN/$SiO_2$ structure. The $r_p(q, \omega)$ can be derived from the Fresnel equations for a three-layer structure shown in Fig. S5:

$$r_p = \frac{r_a + r_s e^{i2k_e^z d}}{1 + r_a r_s e^{i2k_e^z d}}, \tag{S5}$$

$$\begin{aligned} r_a &= \frac{\varepsilon_\perp k_a^z - \varepsilon_a k_e^z}{\varepsilon_\perp k_a^z + \varepsilon_a k_e^z} \\ r_s &= \frac{\varepsilon_s k_e^z - \varepsilon_\perp k_s^z}{\varepsilon_s k_e^z + \varepsilon_\perp k_s^z} \end{aligned}, \tag{S6}$$

where the subscripts "$a$", "$\perp$" and "$s$" refer to air, hBN (the component normal to the $c$-axis), and $SiO_2$, respectively. Functions $r_a$ and $r_s$ have the meaning of the reflectivity of the air/hBN and hBN/$SiO_2$ interfaces, $d$ is the thickness of the hBN crystal and $k_i^z$ represents the $z$-axis

momentum of the photon in layer *i*. For *i* = *a* and *s*, it is given by $k_i^z = \sqrt{\varepsilon_i \frac{\omega^2}{c^2} - q^2}$ with $\varepsilon_i$ being the dielectric function. The subscript "*e*" stands for "extraordinary ray" of hBN, which has uniaxial anisotropy. The corresponding momentum is $k_e^z = \sqrt{\varepsilon_\perp (\omega/c)^2 - \frac{\varepsilon_\perp}{\varepsilon_{//}} q^2}$ (*41*).

4. Derivation of Eq. 1 and the origin of the multiple polariton branches

At large *q* we can make the approximation $k_a^z \approx k_s^z \approx iq$ and

$$k_e^z = iq \frac{\sqrt{\varepsilon_\perp}}{\sqrt{\varepsilon_{//}}} = \frac{q}{\psi}, \tag{S7}$$

in the preceding formulas, which enables us to further simplify the expression for $r_p$. Using straightforward algebraic manipulations, one is led to the analytic solution for the poles of $r_p$, Eq. 1 of the main text. Alternatively, a more physical derivation can be offered as follows. If dissipation is neglected, so that both $\varepsilon_\perp$ and $\varepsilon_{//}$ are real, the admissible value of momentum $k_e^z$ obey the Fabry-Perot quantization condition

$$2k_e^z d + 2\phi_a + 2\phi_s = 2\pi m, \tag{S8}$$

where $2\phi_a$ and $2\phi_s$ are the phases of the reflection coefficients $r_a$ and $-r_s$, i.e.,. the phase shifts for (inner) reflection of the extraordinary ray at the hBN-air and hBN-substrate interfaces. From Eq. S5 and Eq. S6 we find

$$\phi_j = \arctan\left(\frac{\varepsilon_j}{\varepsilon_\perp \psi}\right), \quad j = a, s. \tag{S9}$$

Combining Eq. S7-S9 we arrive at

$$q = -\frac{\psi}{d}(-\pi m + \phi_a + \phi_s). \tag{S10}$$

It is convenient to define $l = -m = 0, 1, \ldots$ to ensure that Re $q > 0$. If the losses are now included, the in-plane momentum would acquire an imaginary part $q \to q + i\kappa$. After these substitutions Eq. S10 becomes the same as the desired result, Eq. 1.

According to Eq. 1, the $0 < \gamma < 1$ condition can be satisfied within the Reststrahlen bands of hBN confined within the transverse $\omega_{TO}$ and longitudinal $\omega_{LO}$ phonon frequencies (Fig. 3D). Our imaging data probe mainly the band due to the upper Reststrahlen band, from $\omega_{TO,\perp}$ = 1367 cm$^{-1}$ to $\omega_{LO,\perp}$ = 1610 cm$^{-1}$ (*26*) where $\varepsilon_\perp$ is real and negative, whereas $\varepsilon_{//}$ is almost real and positive. The polariton branches all start at $\omega_{TO,\perp}$ at low *q* and disperse with the positive slope ($\alpha = +$) towards the limiting value of $\omega_{LO,\perp}$ = 1610 cm$^{-1}$ at large *q*.

Instead of looking for the poles of $r_p$ in the complex plane, one can determine the polariton dispersion from the maxima of Im $r_p$ at real momenta. This numerical method gives results that closely agree with our analytical Eq. 1 at large *q* where the latter equation is valid, see Fig. 2E. The positions of high-intensity lines in this plot give $q$, while their apparent widths characterize the dissipation $\kappa$ (*10*).

Let us now briefly discuss the multiple branches of the polariton dispersion. As explained above, the $l > 0$ branches have a simple interpretation as the Fabry-Perot resonances confined between the two interfaces of the hBN crystal. The same phenomenon occurs in planar waveguides, so these modes can be termed "waveguide modes" (*29*). In our case the polariton branches are separated from one another by equal increments $\frac{\pi\psi}{d}$ in the momentum space. It is unusual however that this number is real while $q$ itself is much larger than the photon momentum. In other words, it is unusual to have propagating modes far outside the light-cone. This fact can be traced to parameter $\psi$ (defined in Eq. 1 or Eq. S7) being real, which is unique to hyperbolic materials such as hBN. Unfortunately, none of the $l > 0$ modes has shown evident features in the experiments so far. Observation of these "waveguide" modes may have been inhibited by imperfections of the sample edges and the current signal/noise ratio limitation.

Finally, it may be worth commenting on applicability of our continuum-medium approach to hBN crystals with just a few atomic layers $N$. Experimentally, our Eq. 1 is seen to be in quantitative agreement with the measurements even in the thinnest samples reported here, $N = 3$. On the theory side, the answer can be gleaned from the theoretical calculations of Michel and Verberck (*42*). They suggest that a qualitatively new effect caused by decrease in the number of layers is the character of yet unobserved high-order polariton branches. These authors find that the total number of all branches is finite and equal to $N$ in each Reststrahlen band. Thus, in monolayer hBN there should be only one and in bilayer only two polariton branches in each band. Since we do not see high-order branches even in thick crystals, this distinction cannot yet be verified.

5. Near field spectra simulation

The near-field scattering amplitude $s(\omega)$ shown in Fig. 2F (right) of the main text was computed using the expression for the reflectivity, which accounted for all possible layers (hBN, $SiO_2$, and Si). It has the same form as Eq. S4 except $r_s$ is replaced by $r_{sq}$:

$$r_{sq} = \frac{r_s + r_q e^{i2k_s^z d_s}}{1 + r_s r_q e^{i2k_s^z d_s}}$$

$$r_q = \frac{\varepsilon_q k_s^{\ z} - \varepsilon_s k_q^{\ z}}{\varepsilon_q k_s^{\ z} + \varepsilon_s k_q^{\ z}} \quad , \qquad \text{(S11)}$$

$$k_q^{\ z} = \sqrt{\varepsilon_q (\frac{\omega}{c})^2 - q^2}$$

where $d_s = 300$ nm is the $SiO_2$ thickness and $\varepsilon_q = 11.7$ is the IR dielectric constant of Si. The tip-sample interaction was treated within the quasi-static approximation in which the AFM tip was modeled as a perfectly conducting prolate spheroid of total length 600 nm and the curvature radius 30 nm, as described in our previous work (*28*). Figure 2F indicates that the modeling captures all the main features of the observed spectrum. Two features arise due to two effects. One is the behavior of the ordinary reflectivity $r_p$ at nearly zero momentum, i.e., the photonic response of our hBN/$SiO_2$/Si system. The other ingredient is the $\omega-$ dependence of $r_p$ at very large momenta $q \sim 10^5$ cm$^{-1}$ set by the curvature radius of the tip and its typical distance from the sample, i.e., the polaritonic effect. The photonic response causes the deep minima at 820 cm$^{-1}$

and 1625 $cm^{-1}$. These minima occur near the longitudinal optical (LO) phonon frequencies of hBN, $\omega_{LO,//}$ and $\omega_{LO,\perp}$ at which the far-field reflectivity $r_p$ is close to −1, see Eq. S11), so that the electric field at the surface, proportional to $1 + r_p$, vanishes. (Note that the far-field reflectivity is a very sharp function of frequency near $\omega_{LO,\perp}$. It rapidly changes from −1 to 0 as frequency increases, giving the well-known reflectivity minimum.) The far-field reflectivity is also responsible for the hump-dip structure near 1100 $cm^{-1}$, which comes from the optical phonon of the $SiO_2$ substrate. On the other hand, the resonances centered around 760 $cm^{-1}$ and 1370 $cm^{-1}$ are to a large extent due to the high *near-field* reflectivity, the raison d'être of the polaritons. The combination of the far- and near-field response functions anchors these peaks at the transverse optical (TO) frequencies.

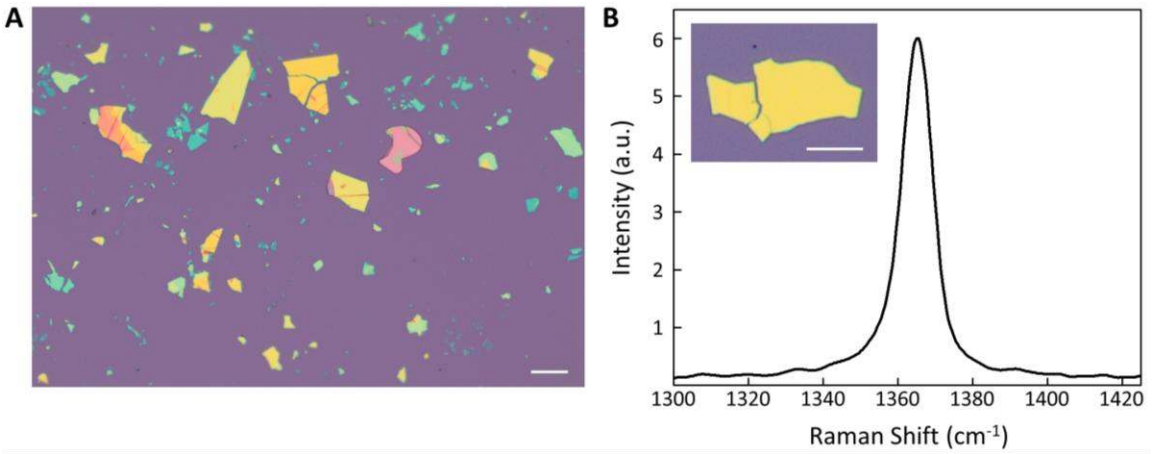


**Fig. S1. Optical microscope image and Raman spectrum of hBN.**

(**A**) hBN crystals of different thicknesses under the optical microscope. (**B**) Raman spectrum of the hBN crystal displayed in the inset. Scale bar: 30μm.

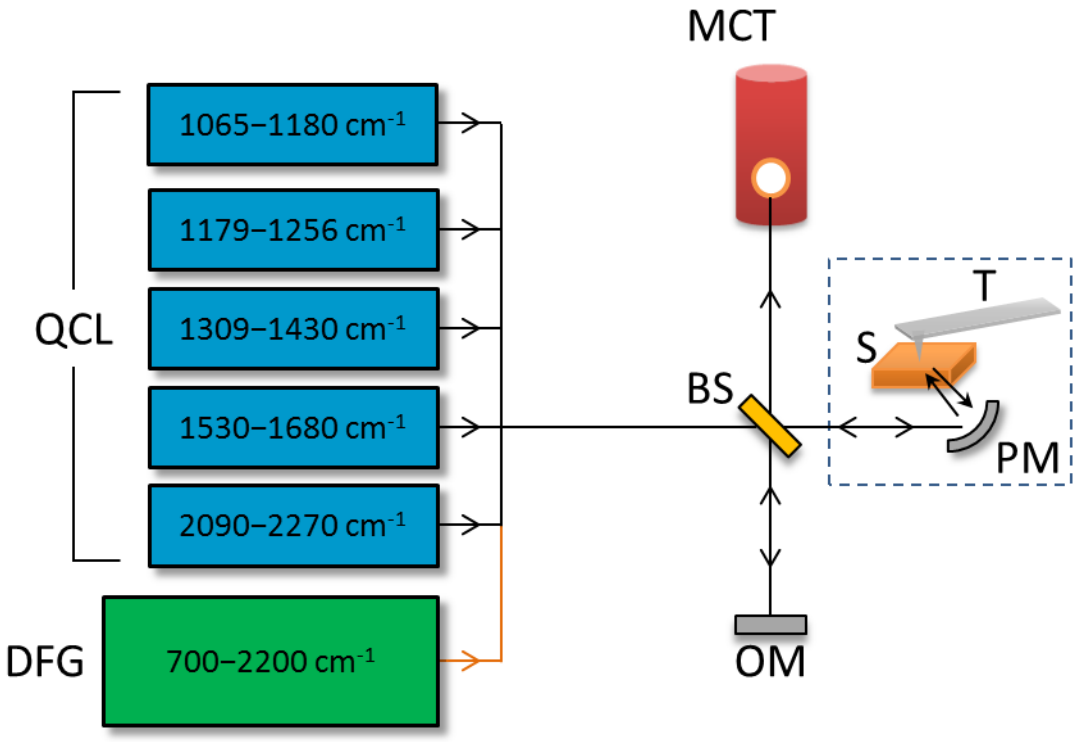


**Fig. S2. Schematics of the UCSD s-SNOM for broad-band nano-imaging and nano-FTIR experiments.**

Single frequency IR light (black arrows) is generated by 5 QCLs with tunable frequency indicated, in $cm^{-1}$. A broad-band beam (orange arrow) is generated by the DFG system with frequency range indicated. The IR beam enters an asymmetric interferometer composed of the elements: BS=ZnSe Beam Splitter, OM=Oscillating Mirror, MCT=Mercury Cadmium Telluride detector, PM=Parabolic Mirror, T=metallized Tip, S=Sample. Dashed box marks the s-SNOM part.

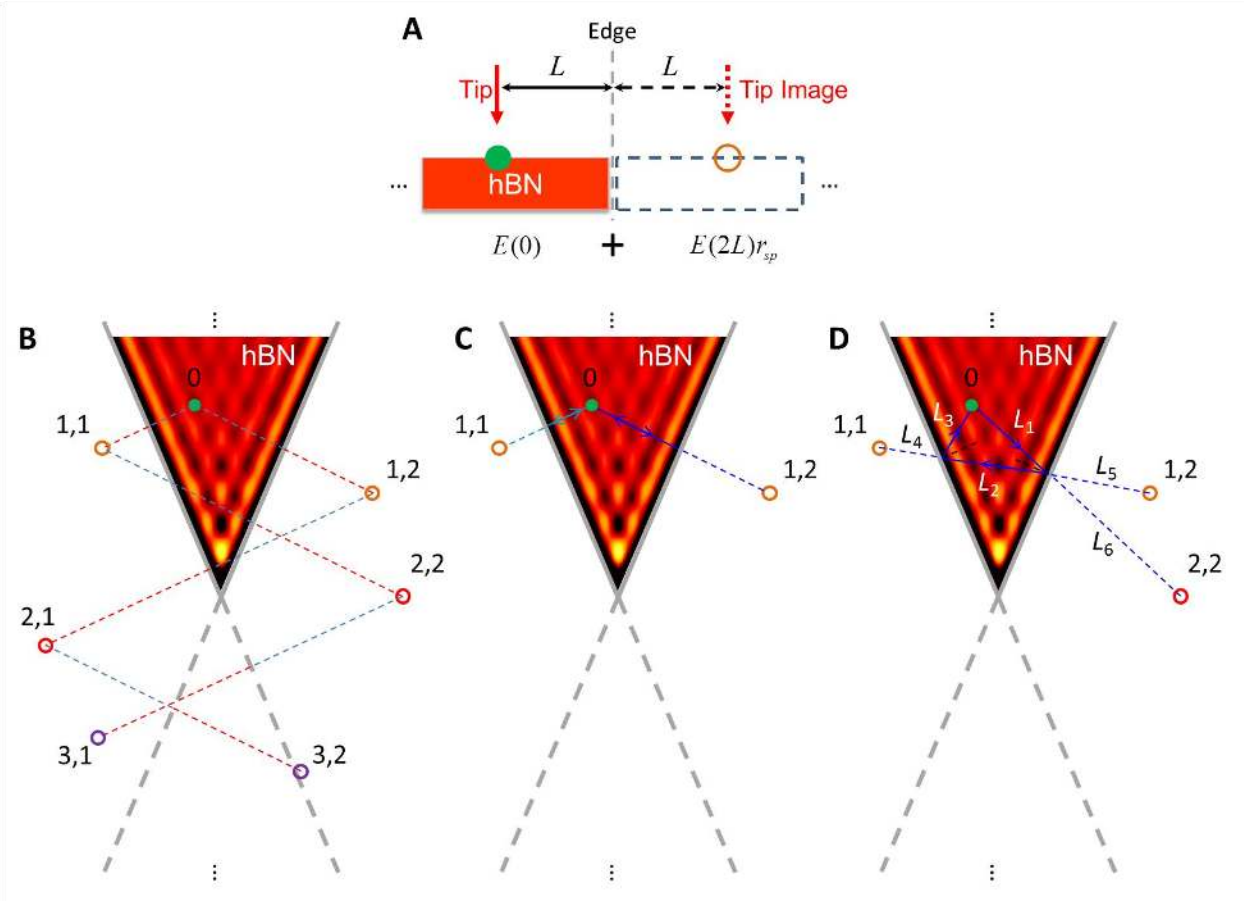


**Fig. S3. Polaritonic waves in tapered crystals.**

(**A**) Tip (solid red arrow) and its mirror image (dashed red arrow) according to the single hBN edge (grey dashed line). (**B**) A representative tip position (solid green dot, noted as "0") and its images (hollow dots, labeled as "*m*,*n*") for the simulation in Fig. 1C. Orange, red and purple dots mark the 1-st, 2-nd and 3-rd order images of the tip, respectively. Solid grey lines track the hBN crystal's edges; their extensions are shown with dashed lines. Red and blue dashed lines symmetrically connect the tip images with respect to the hBN edges. (**C**) The beam path (solid lines with arrow) of the 1-st order polariton waves. (**D**) The beam path (solid lines with arrow) of one representative 2-nd order polariton wave. $L_1$ to $L_6$ represent the length of each part in the solid (or dashed) blue line. Color map of (B-D): simulation results from Fig. 1C.

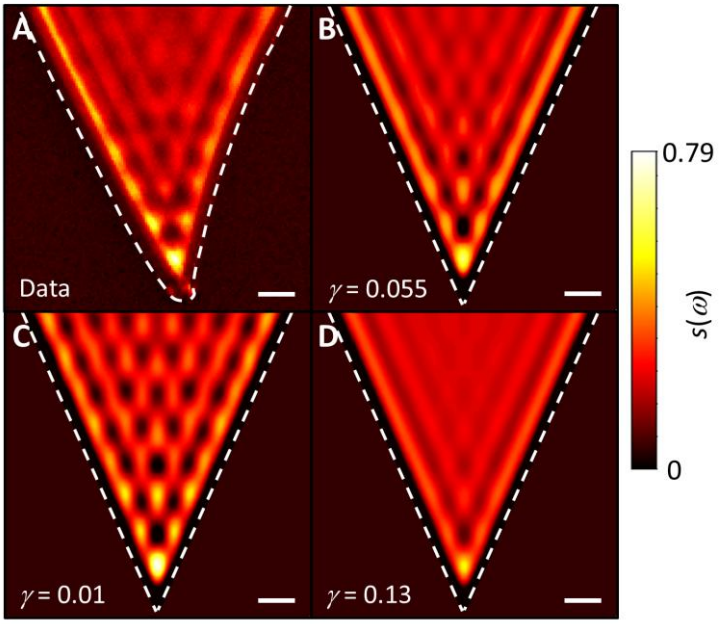


**Fig. S4. Near-field image and simulation results with different loss factors.**

(**A**) Near-field image of phonon polaritons from Fig. 1B of the main text. (**B**) Simulation image with the loss factor $\gamma = 0.055$ (Fig. 1C). (**C**) Simulation image with the loss factor $\gamma = 0.01$. (**D**) Simulation image with the loss factor $\gamma = 0.13$. Scale bar: 800 nm in all panels.


Fig. S5. Layered structure for the Air-hBN-$SiO_2$ system of the dispersion model.

**References and Notes**


1. C. R. Dean, A. F. Young, I. Meric, C. Lee, L. Wang, S. Sorgenfrei, K. Watanabe, T. Taniguchi, P. Kim, K. L. Shepard, J. Hone, Boron nitride substrates for high-quality graphene electronics. *Nat. Nanotechnol.* **5**, 722–726 (2010). Medline doi:10.1038/nnano.2010.172

2. K. S. Novoselov, D. Jiang, F. Schedin, T. J. Booth, V. V. Khotkevich, S. V. Morozov, A. K. Geim, Two-dimensional atomic crystals. *Proc. Natl. Acad. Sci. U.S.A.* **102**, 10451–10453 (2005). Medline doi:10.1073/pnas.0502848102

3. A. K. Geim, I. V. Grigorieva, Van der Waals heterostructures. *Nature* **499**, 419–425 (2013). Medline doi:10.1038/nature12385

4. T. Kimura, Y. Tokura, Layered magnetic manganites. *Annu. Rev. Mater. Sci.* **30**, 451–474 (2000). doi:10.1146/annurev.matsci.30.1.451

5. K. F. Mak, C. Lee, J. Hone, J. Shan, T. F. Heinz, Atomically thin $MoS_2$: A new direct-gap semiconductor. *Phys. Rev. Lett.* **105**, 136805 (2010). Medline doi:10.1103/PhysRevLett.105.136805

6. A. Splendiani, L. Sun, Y. Zhang, T. Li, J. Kim, C. Y. Chim, G. Galli, F. Wang, Emerging photoluminescence in monolayer $MoS_2$. *Nano Lett.* **10**, 1271–1275 (2010). Medline doi:10.1021/nl903868w

7. X. Qi, S. Zhang, Topological insulators and superconductors. *Rev. Mod. Phys.* **83**, 1057–1110 (2011). doi:10.1103/RevModPhys.83.1057

8. L. Britnell, R. M. Ribeiro, A. Eckmann, R. Jalil, B. D. Belle, A. Mishchenko, Y.-J. Kim, R. V. Gorbachev, T. Georgiou, S. V. Morozov, A. N. Grigorenko, A. K. Geim, C. Casiraghi, A. H. Castro Neto, K. S. Novoselov, Strong light-matter interactions in heterostructures of atomically thin films. *Science* **340**, 1311–1314 (2013); 10.1126/science.1235547. Medline doi:10.1126/science.1235547

9. S. Z. Butler, S. M. Hollen, L. Cao, Y. Cui, J. A. Gupta, H. R. Gutiérrez, T. F. Heinz, S. S. Hong, J. Huang, A. F. Ismach, E. Johnston-Halperin, M. Kuno, V. V. Plashnitsa, R. D. Robinson, R. S. Ruoff, S. Salahuddin, J. Shan, L. Shi, M. G. Spencer, M. Terrones, W. Windl, J. E. Goldberger, Progress, challenges, and opportunities in two-dimensional materials beyond graphene. *ACS Nano* **7**, 2898–2926 (2013). Medline doi:10.1021/nn400280c

10. L. Novotny, B. Hecht, *Principles of Nano-Optics* (Cambridge Univ. Press, Cambridge, 2006).

11. J. Renger, S. Grafström, L. M. Eng, R. Hillenbrand, Resonant light scattering by near-field-induced phonon polaritons. *Phys. Rev. B* **71**, 075410 (2005). doi:10.1103/PhysRevB.71.075410

12. S. Shen, A. Narayanaswamy, G. Chen, Surface phonon polaritons mediated energy transfer between nanoscale gaps. *Nano Lett.* **9**, 2909–2913 (2009). Medline doi:10.1021/nl901208v

13. T. Feurer, J. C. Vaughan, K. A. Nelson, Spatiotemporal coherent control of lattice vibrational waves. *Science* **299**, 374–377 (2003). Medline doi:10.1126/science.1078726

14. Y. De Wilde, F. Formanek, R. Carminati, B. Gralak, P. A. Lemoine, K. Joulain, J. P. Mulet, Y. Chen, J. J. Greffet, Thermal radiation scanning tunnelling microscopy. *Nature* **444**, 740–743 (2006). Medline doi:10.1038/nature05265

15. A. Huber, N. Ocelic, D. Kazantsev, R. Hillenbrand, Near-field imaging of mid-infrared surface phonon polariton propagation. *Appl. Phys. Lett.* **87**, 081103 (2005). doi:10.1063/1.2032595

16. T. Taubner, D. Korobkin, Y. Urzhumov, G. Shvets, R. Hillenbrand, Near-field microscopy through a SiC superlens. *Science* **313**, 1595 (2006). Medline doi:10.1126/science.1131025

17. G. Shvets, Photonic approach to making a material with a negative index of refraction. *Phys. Rev. B* **67**, 035109 (2003). doi:10.1103/PhysRevB.67.035109

18. J. A. Schuller, R. Zia, T. Taubner, M. L. Brongersma, Dielectric metamaterials based on electric and magnetic resonances of silicon carbide particles. *Phys. Rev. Lett.* **99**, 107401 (2007). Medline doi:10.1103/PhysRevLett.99.107401

19. Materials and methods are available as supplementary materials on *Science* Online.

20. J. Chen, M. Badioli, P. Alonso-González, S. Thongrattanasiri, F. Huth, J. Osmond, M. Spasenović, A. Centeno, A. Pesquera, P. Godignon, A. Z. Elorza, N. Camara, F. J. García de Abajo, R. Hillenbrand, F. H. Koppens, Optical nano-imaging of gate-tunable graphene plasmons. *Nature* **487**, 77–81 (2012). Medline

21. Z. Fei, A. S. Rodin, G. O. Andreev, W. Bao, A. S. McLeod, M. Wagner, L. M. Zhang, Z. Zhao, M. Thiemens, G. Dominguez, M. M. Fogler, A. H. Castro Neto, C. N. Lau, F. Keilmann, D. N. Basov, Gate-tuning of graphene plasmons revealed by infrared nano-imaging. *Nature* **487**, 82–85 (2012). Medline

22. F. Keilmann, S. Amarie, Mid-infrared frequency comb spanning an octave based on an Er fiber laser and difference-frequency generation. *J. Infrared Millimeter Terahertz Waves* **33**, 479–484 (2012). doi:10.1007/s10762-012-9894-x

23. J. M. Atkin, S. Berweger, A. C. Jones, M. B. Raschke, Nano-optical imaging and spectroscopy of order, phases, and domains in complex solids. *Adv. Phys.* **61**, 745–842 (2012). doi:10.1080/00018732.2012.737982

24. Z. Fei, G. O. Andreev, W. Bao, L. M. Zhang, A. S McLeod, C. Wang, M. K. Stewart, Z. Zhao, G. Dominguez, M. Thiemens, M. M. Fogler, M. J. Tauber, A. H. Castro-Neto, C. N. Lau, F. Keilmann, D. N. Basov, Infrared nanoscopy of dirac plasmons at the graphene-$SiO_2$ interface. *Nano Lett.* **11**, 4701–4705 (2011). Medline doi:10.1021/nl202362d

25. R. Hillenbrand, T. Taubner, F. Keilmann, Phonon-enhanced light matter interaction at the nanometre scale. *Nature* **418**, 159–162 (2002). Medline doi:10.1038/nature00899

26. R. Geick, C. H. Perry, G. Rupprecht, Normal modes in hexagonal boron nitride. *Phys. Rev.* **146**, 543–547 (1966). doi:10.1103/PhysRev.146.543

27. X. G. Xu, A. E. Tanur, G. C. Walker, Phase controlled homodyne infrared near-field microscopy and spectroscopy reveal inhomogeneity within and among individual boron nitride nanotubes. *J. Phys. Chem. A* **117**, 3348–3354 (2013). Medline doi:10.1021/jp4008784

28. L. M. Zhang, G. O. Andreev, Z. Fei, A. S. McLeod, G. Dominguez, M. Thiemens, A. H. Castro-Neto, D. N. Basov, M. M. Fogler, Near-field spectroscopy of silicon dioxide thin films. *Phys. Rev. B* **85**, 075419 (2012). doi:10.1103/PhysRevB.85.075419

29. A. Poddubny, I. Iorsh, P. Belov, Y. Kivshar, Hyperbolic metamaterials. *Nat. Photonics* **7**, 948–957 (2013). doi:10.1038/nphoton.2013.243

30. R. Stanley, Plasmonics in the mid-infrared. *Nat. Photonics* **6**, 409–411 (2012). doi:10.1038/nphoton.2012.161

31. K. Watanabe, T. Taniguchi, H. Kanda, Direct-bandgap properties and evidence for ultraviolet lasing of hexagonal boron nitride single crystal. *Nat. Mater.* **3**, 404–409 (2004). Medline doi:10.1038/nmat1134

32. R. V. Gorbachev, I. Riaz, R. R. Nair, R. Jalil, L. Britnell, B. D. Belle, E. W. Hill, K. S. Novoselov, K. Watanabe, T. Taniguchi, A. K. Geim, P. Blake, Hunting for monolayer boron nitride: Optical and Raman signatures. *Small* **7**, 465–468 (2011). Medline doi:10.1002/smll.201001628

33. D. Golla, K. Chattrakun, K. Watanabe, T. Taniguchi, B. J. LeRoy, A. Sandhu, Optical thickness determination of hexagonal boron nitride flakes. *Appl. Phys. Lett.* **102**, 161906 (2013). doi:10.1063/1.4803041

34. S. V. Ordin, B. N. Sharupin, M. I. Fedorov, Normal lattice vibrations and the crystal structure of anisotropic modifications of boron nitride. *Semiconductors* **32**, 924–932 (1998). doi:10.1134/1.1187516

35. E. Franke, M. Schubert, H. Neumann, T. E. Tiwald, D. W. Thompson, J. A. Woollam, J. Hahn, F. Richter, Phase and microstructure investigations of boron nitride thin films by spectroscopic ellipsometry in the visible and infrared spectral range. *J. Appl. Phys.* **82**, 2906 (1997). doi:10.1063/1.366123

36. E. Franke, M. Schubert, J.-D. Hecht, H. Neumann, T. E. Tiwald, D. W. Thompson, H. Yao, J. A. Woollam, J. Hahn, *In situ* infrared and visible-light ellipsometric investigations of boron nitride thin films at elevated temperatures. *J. Appl. Phys.* **84**, 526 (1998). doi:10.1063/1.368083

37. Y. Cai, L. Zhang, Q. Zeng, L. Cheng, Y. Xu, Infrared reflectance spectrum of BN calculated from first principles. *Solid State Commun.* **141**, 262–266 (2007). doi:10.1016/j.ssc.2006.10.040

38. N. Ohba, K. Miwa, N. Nagasako, A. Fukumoto, First-principles study on structural, dielectric, and dynamical properties for three BN polytypes. *Phys. Rev. B* **63**, 115207 (2001). doi:10.1103/PhysRevB.63.115207

39. T. Kuzuba, K. Era, T. Ishii, T. Sato, A low frequency Raman-active vibration of hexagonal boron nitride. *Solid State Commun.* **25**, 863–865 (1978). doi:10.1016/0038-1098(78)90288-0

40. R. J. Nemanich, S. A. Solin, R. M. Martin, Light scattering study of boron nitride microcrystals. *Phys. Rev. B* **23**, 6348–6356 (1981). doi:10.1103/PhysRevB.23.6348

41. J. Lekner, Reflection ellipsometry of uniaxial crystals. *J. Opt. Soc. Am. A Opt. Image Sci. Vis.* **14**, 1359 (1997). doi:10.1364/JOSAA.14.001359

42. K. H. Michel, B. Verberck, Theoretical phonon dispersions in monolayers and multilayers of hexagonal boron-nitride. *Phys. Status Solidi B* **246**, 2802–2805 (2009). doi:10.1002/pssb.200982307